Magnetic Transition in Exotic Perovskites Stabilized by Chemical and Physical Pressure

Journal:	*Journal of Materials Chemistry C*
Manuscript ID	TC-ART-12-2019-006976.R2
Article Type:	Paper
Date Submitted by the Author:	26-Feb-2020
Complete List of Authors:	Ma, Yalin; Sun Yat-Sen University, School of Chemistry Molokeev, Maxim S. ; Kirensky Institute of Physics SB RAS; Siberian Federal University; Far Eastern State Transport University, Department of Physics Zhu, Chuanhui; Sun Yat-Sen University, School of Chemistry Zhao, Shuang; Sun Yat-Sen University, School of Chemistry Han, Yi-Feng; Key Laboratory of Bioinorganic and Synthetic Chemistry of Ministry of Education, School of Chemistry, Sun Yat-Sen University Wu, Meixia ; School of Chemistry, Sun Yat-Sen University, Liu, Sizhan; New Jersey Institute of Technology, Physics Tyson, Trevor; NJIT, Croft, Mark ; Rutgers, The State University of New Jersey Li, Man-Rong; Sun Yat-Sen University, School of Chemistry

ARTICLE

Magnetic Transitions in Exotic Perovskites Stabilized by Chemical and Physical Pressure

Yalin Ma,[a] Maxim S. Molokeev,[b,c,d] Chuanhui Zhu,[a] Shuang Zhao,[a] Yifeng Han,[a] Meixia Wu,[a] Sizhan Liu,[e] Trevor A. Tyson,[e] Mark Croft[f] and Man-Rong Li*,[a]

Received 00th January 20xx,
Accepted 00th January 20xx

DOI: 10.1039/x0xx00000x

Exotic Perovskites significantly enrich materials in multiferroic and magnetoelectric applications. However, their design and synthesis is a challenge due to the mostly required recipe conditions at extremely high pressure. Herein, we presented the $Ca_{2-x}Mn_xMnTaO_6$ ($0 \le x \le 1.0$) solid solutions stabilized by chemical pressure assisted with intermediate physical pressure up to 7 GPa. The incorporation of Mn^{2+} into the *A*-site neither drives any cationic ordering nor modifies the orthorhombic *Pbnm* structure, namely written as $(Ca_{1-x/2}Mn_{x/2})(Mn_{1/2}Ta_{1/2})O_3$ with disordered *A* and *B* site cationic arrangements. The increment of *x* is accompanied by a ferromagnetic to antiferromagnetic transition around $x = 0.2$, which is attributed to the double-exchange interactions between *A*-site Mn^{2+} and *B*-site Mn^{3+}. Partial charge disproportionation of the *B*-site Mn^{3+} into Mn^{2+} and Mn^{4+} occurs for *x* above 0.8 samples as manifested by X-ray spectrum and magnetic behaviors. The coexistence of *B*-site Mn^{3+} (Jahn-Teller distortion ion) and *B*′-site Ta^{5+} (second-order Jahn-Teller distortion ion) could be energetically responsible for the absence of *A*-site columnar ordering as observed in other quadruple perovskites with half of the *A*-sites occupied by small transition-metal cations. These exceptional findings indicate that exotic perovskites can be successfully stabilized at chemical and intermediate physical pressure, and the presence of Jahn-teller distortion cations at the same lattice should be avoided to enable cationic ordering.

Introduction

Perovskite oxides have attracted great interest because of their enriched structural, magnetic, and electronic properties.[1-4] The stability and crystal system of ABO_3 perovskites can be depicted by the octahedral factor $\mu = r_B/r_O$ and tolerance factor $t = (r_A + r_O)/\sqrt{2}(r_B + r_O)$ proposed by Goldschmidt (r_i stands for the ionic radius of ion *i*).[5, 6] The radii of ions and tilting of octahedron have a significant impact on stabilizing perovskite structure in light of their chemical, octahedral, stretch, and tilt limits.[7-12] In contrast to conventional perovskite with large *A*-site cations, the exotic perovskite can adaptively incorporate small cations (especially transition-metal ions) into the *A*-site.[13-16] *A*-site columnar-ordered quadruple perovskites $A_2A'A''B_4O_{12}$ with 50% of the small *A*-sites (denoted as square-planar coordinated *A*′ and tetrahedrally coordinated *A*′′, respectively) was firstly discovered in $Ca_2Fe'Fe''Ti_4O_{12}$ (also known as $CaFeTi_2O_6$ with $A' = A'' = Fe$)[17] and then $Ca_2Mn'Mn''Ti_4O_{12}$ (known as $CaMnTi_2O_6$ with $A' = A'' = Mn$).[18] $Ca_2Fe'Fe''Ti_4O_{12}$ crystallizes in centrosymmetric *P*4₂/*nmc* (No. 137), while $Ca_2Mn'Mn''Ti_4O_{12}$ adopts a polar *P*4₂*mc* (No. 105) structure in that Mn′ displaces off from the $Mn'O_4$ square-plane (**Fig. 1a**) other than exactly stays in the oxygen plane as observed for Fe′ in $Fe'O_4$ of $Ca_2Fe'Fe''Ti_4O_{12}$.[19] Rock-salt *B*-site ordering in $A_2A'A''B_2B'_2O_{12}$ (**Fig. 1b**) provides higher compositional freedom as reported in the *P*4₂/*n* (No. 86) type $Ca_2Mn'Mn''B_2Re_2O_{12}$ (*B* = Mn,[20] Fe,[20] Co,[21] Ni[21]), $Ca_2Mn^{A'}Cu^{A''}(Fe_2)^{B}(Re_2)^{B'}O_{12}$,[20] and $R_2Mn'Mn''Mn_2Sb_2O_{12}$ (*R* = La, Pr, Nd, Sm).[22] The $A'O_4$ (square-planar), $A''O_4$ (tetrahedral), BO_6 (octahedral), and $B'O_6$ (octahedral) sites in $A_2A'A''B_2B'_2O_{12}$ are highly adaptable,[23] and can be occupied by the same element as recently observed in RMn_3O_6 (*R* = Y, Gd, Dy, Ho, Er, Tm; $A' = A'' = B = B' = Mn$),[24-26] which crystallize in *Pmmn* (No. 59, **Fig. 1c**) and can be structurally written as $R^{3+}_2(Mn^{2+})^{A'}(Mn^{3+})^{A''}(Mn^{3+})_2{}^{B}(Mn^{3.5+})_2{}^{B'}O_{12}$ with layered charge ordering over the *B*-sites. When 75% of the *A*-sites are occupied by small cations, $AA'_3B_4O_{12}$-type quadruple perovskites can be formed with square-planar coordinated *A*′-site, such as $A' = Mn^{3+}$, Co^{2+}, Cu^{2+}, Pd^{2+} in $LaMn_3V_4O_{12}$,[27] $LaCu_3Fe_4O_{12}$,[28] $CaCo_3V_4O_{12}$,[29, 30] $CaPd_3Ti_4O_{12}$,[31, 32] respectively. Most known $AA'_3B_4O_{12}$ quadruple perovskites are in cubic *Im*-3 (No. 204) symmetry (**Fig. 1d**) unless the *B*-site charge-ordering induced distortion occurs as in rhombohedral manganite $A^{2+}Mn_3Mn_4O_{12}$ (*R*-3, No. 148, *A* = Ca, Cd, Pb, Pr, Sr, **Fig. 1e**).[33-35] 1322-type *B*-site ordering of quadruple perovskites $AA'_3B_2B'_2O_{12}$ leads to a

---

[a] Key Laboratory of Bioinorganic and Synthetic Chemistry of Ministry of Education, School of Chemistry, Sun Yat-Sen University, Guangzhou 510275, China
[b] Laboratory of Crystal Physics, Kirensky Institute of Physics, Federal Research Center KSC SB RAS, Krasnoyarsk 660036, Russia
[c] Siberian Federal University, Krasnoyarsk 660041, Russia
[d] Department of Physics, Far Eastern State Transport University, Khabarovsk 680021, Russia
[e] Department of Physics, New Jersey Institute of Technology, Newark, New Jersey 07102, United States
[f] Department of Physics & Astronomy, Rutgers, The State University of New Jersey, 136 Frelinghuysen Road, Piscataway, New Jersey 08854, United States
Email: limanrong@mail.sysu.edu.cn

Electronic Supplementary Information (ESI) available: CSD 1972419, CSD 1972420, CSD 1972421 and CSD 1972422. For ESI and crystallographic data in CIF or other electronic format see DOI: 10.1039/x0xx00000x

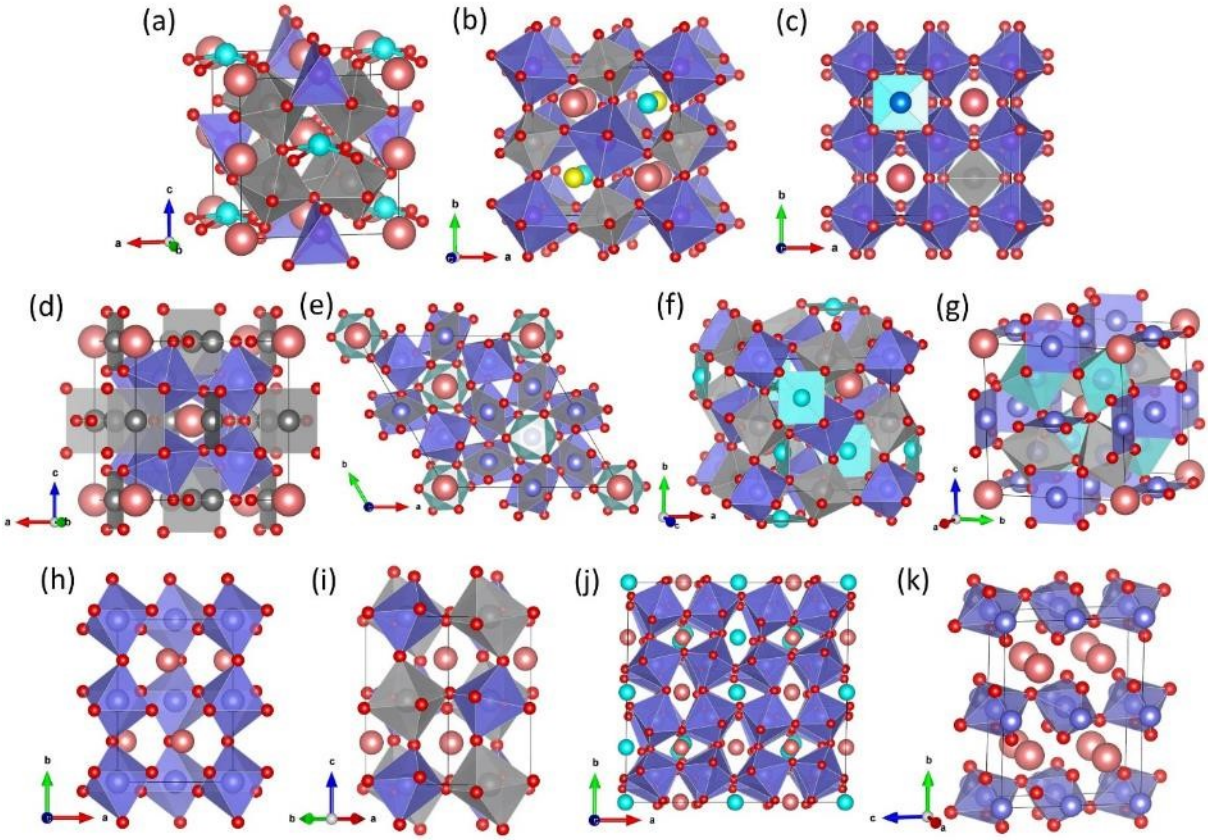

Fig. 1 Crystal structures of exotic perovskite oxides with small *A*-site cations. *A*, pink spheres; O, red spheres; BO_6 octahedra, violet; $B'O_6$ octahedra, silver gray; a_p is the lattice parameter of simple cubic perovskite. $A_2A'A''B_4O_{12}$ with 50% of the small cationic *A*-sites (*A'* and *A''*): (**a**) *A*-site columnar-ordered quadruple perovskites $A_2A'A''B_4O_{12}$ (tetragonal, $P4_2mc$, $2a_p \times 2a_p \times 2a_p$ type). $A'O_4$ square-planar, cyan; $A''O_4$ tetrahedral, violet; BO_6 octahedra, silver gray. (**b**) Rock-salt *B*-sites ordering in $A_2A'A''B_2B'_2O_{12}$ (tetragonal, $P4_2/n$, $2a_p \times 2a_p \times 2a_p$ type). *A'*, cyan spheres; *A''*, yellow spheres. (**c**) RMn_3O_6 with layered charge ordering over the *B*-sites (orthorhombic, *Pmmn*, $2a_p \times 2a_p \times 2a_p$ type). $Mn1O_4$ square-planar, cyan; $Mn2O_4$ tetrahedral, silver gray; MnO_6 octahedra, violet. $AA'_3B_4O_{12}$ with 75% of small cationic *A*-sites (*A'*): (**d**) Most known $AA'_3B_4O_{12}$ quadruple perovskites (cubic, *Im*-3, $2a_p \times 2a_p \times 2a_p$ type). $A'O_4$ square-planar, silver gray. (**e**) *B*-site charge-ordering of $A^{2+}Mn_3Mn_4O_{12}$ (rhombohedral, *R*-3, as the subgroup of $a_p \times 2a_p \times 2a_p$ type *Im*-3). $Mn1O_4$ square-planar, silver gray; $Mn2O_6$ octahedra, violet; $Mn3O_6$ octahedra, cyan. (**f**) 1322-type *B*-site ordering of $AA'_3B_2B'_2O_{12}$ (cubic, *Pn*-3, $2a_p \times 2a_p \times 2a_p$ type). $A'O_4$ square-planar, cyan. (**g**) Trivalent *A*-site driving Jahn-Teller distorted Mn^{3+} component on the *B*-site of $A^{3+}Mn_7O_{12}$ (monoclinic, *I*2/*m*, $2a_p \times 2a_p \times 2a_p$ type), MnO_4 square-planar, violet; $Mn4O_6$ octahedra, silver gray; $Mn5O_6$ octahedra, cyan. Exotic perovskite with 100% of small cationic *A*-sites: (**h**) $GdFeO_3$-based ABO_3-type (orthorhombic, *Pbnm*, $\sqrt{2}a_p \times \sqrt{2}a_p \times 2a_p$ type); (**i**) $A_2BB'O_6$ -type (monoclinic, $P2_1/n$, $\sqrt{2}a_p \times \sqrt{2}a_p \times 2a_p$ type), (**j**) ζ-Mn_2O_3-type (triclinic, *F*-1, $4a_p \times 4a_p \times 4a_p$ type), and (**k**) Post-perovskite (orthorhombic, *Cmcm*, $\sqrt{2}a_p/2 \times 2a_p \times \sqrt{3}a_p$ type).

symmetry evolution from *Im*-3 to *Pn*-3 (No. 201, **Fig. 1f**) such as reported in $CaCu_3Fe_2Re_2O_{12}$,[36] $CaCu_3Fe_2Nb_2O_{12}$,[37] and $NaCu_3Fe_2Os_2O_{12}$.[38] In $A^{3+}Mn_7O_{12}$ (*A* = La, Pr, Nd) series the trivalent *A*-site ion drives more Jahn-Teller distorted Mn^{3+} component on the *B*-site, which, together with charge ordering, results in monoclinic *I*2/*m* (No. 12) structure (**Fig. 1g**) as in $Pr^{3+}Mn^{3+}_3(Mn^{2.99+})^{B}{}_2(Mn^{3.01+})^{B'}{}_2O_{12}$.[39, 40] The spatial effect of $6s^2$-lone pair electrons of Bi^{3+} in $BiMn_7O_{12}$ further leads to complex temperature-dependent symmetry evolution of *Im*-3 (above 608 K) - *I*2/m (460-608 K) - *Im* (290-460 K) - *P*1 (below 290 K) upon cooling.[41] Full occupation of the *A*-site with small cations usually draws pressure-dependent polymorph competition, and mostly the perovskite phases need to be stabilized from higher pressure synthesis.[16, 42-44] $GdFeO_3$-based *Pnma* (No. 62, **Fig. 1h**) and $P2_1/n$ (No. 14) structures (**Fig. 1i**) have been successively discovered in ABO_3-type (such as $MnVO_3$ and $ScCrO_3$)[45-47] and $A_2BB'O_6$ -type (such as Mn_2BSbO_6 (*B* = Fe,[43] Sc,[48]V[49]), Mn_2BReO_6 (*B* = Mn,[14, 50] Fe,[15, 51] Co[52]), and $Mn_2(Fe_{0.8}Mo_{0.2})MoO_6$)[13]) perovskites, respectively. $AA'_3B_4O_{12}$-type quadruple perovskites can also be prepared in this category if the pressure is high enough, such as $ACu_3V_4O_{12}$ (*Im*-3, *A* = Cu, Mn), and ζ-Mn_2O_3 (structurally written as $Mn^{2+}(Mn^{3+})_3(Mn^{3.25+})_4O_{12}$, **Fig. 1j**, *P*-1 (No. 2)).[53-55] Post-perovskite structural compounds (**Fig. 1k**, *Cmcm*, No. 63) such as δ-Mn_2O_3 and $MgSiO_3$ can exist at extremely high pressure but unquenchable to ambient conditions.[56, 57]

Partial or full occupation of small cations on the *A*-site in exotic perovskite not only depicts an enriched image of structural chemistry, but also provides a continuous impetus to search for emergent physical properties, in that the small *A*-site cations, especially transition-metal ions, enhance the quantum degree of freedom such as lattice, spin, charge, and orbital. The reduced *t* can cause structural distortion and thus large spontaneous electrical polarization (P_S) in noncentrosymmetric materials ,[58, 59] while the transition-metal-rich lattices lead to robust magnetic interplays and thus magnetoelectric effect.[15, 28, 51] For examples, $CaMnTi_2O_6$ is the only lone-pair-electron free switchable ferroelectric double perovskite (P_S ~ 24 μC/cm^2),[18] demonstrating potential piezoelectric and ferroelectric-photovoltaic applications; $Ca_2Mn^{A'}Cu^{A''}(Fe_2)^{B}(Re_2)^{B'}O_{12}$ is an above room-temperature ferromagnet (Curie temperature T_C of 560 K) with large room-temperature magnetizations and low-temperature switchable magnetoresistance;[20] $LaCu_3Fe_4O_{12}$ undergoes a temperature-dependent charge transfer around 400 K, accompanied by a metal-insulator transition behavior;[28] $CaCu_3Fe_2Re_2O_{12}$ is a ferrimagnetic (T_C ~ 560 K) half metal with large saturated magnetization of 8.7 μ_B;[36] Mn_2FeReO_6 displays giant positive magnetoresistance up to 220%;[15, 51] ζ-Mn_2O_3 is the hardest direct narrow bandgap semiconductor, showing switchable *p-n* electronical conduction and spin-induced multiferroicity.[53-55] This list can be even longer. However, these exotic perovskites are thermodynamically metastable and need to be prepared at high-pressure (usually above 6 GPa) and temperature (HPT). This costly procedure and small-scale sample amount (usually milligram level) significantly limit the applications of these materials. Therefore, synthesis at ambient or much lower pressure, which remains a challenge, is highly desired.

Recently, Zhou *et al.* successfully stabilized gram-level high-pressure $Ca_{2-x}Mn_xTi_2O_6$ ($x \leq 0.6$) phase under a very modest pressure (below 0.1 GPa).[19] $Ca_{1.4}Mn_{0.6}Ti_2O_6$ is isostructural with $CaMnTi_2O_6$ ($P4_2mc$) and shows similarly high ferroelectric transition temperature. These findings suggest that it is possible to achieve large-scale high-pressure product driven by chemical potential (pressure)[60] and very modest physical pressure. Understandably, Ca^{2+} and Mn^{2+} have the same charge and slightly different ionic radii (at eight coordination, ${}^{VIII}r(Ca^{2+})$ = 1.12 Å, ${}^{VIII}r(Mn^{2+})$ = 0.96 Å),[61] so that the chemical pressure can assist to underpin Mn^{2+} into the Ca^{2+} matrix. In this work, we reported the perovskite solid solution of $Ca_{2-x}Mn_xMnTaO_6$ ($0 \leq x \leq 1.0$) stabilized by the combination of chemical and physical pressure, and intensively studied the composition-dependent evolution of the crystal structure, formal oxidation states of cations, and magnetic properties.

Experimental

Synthesis

The Ca_2MnTaO_6 (CMTO) precursor was prepared by solid-state reactions with appropriate stoichiometric amount of $CaCO_3$ (MACKLIN, 99.99%), Mn_2O_3 (Sigma-Aldrich, 99.99%), and Ta_2O_5 (Alfa Aesar, 99.993%). The mixture was ground and pressed into pellets, calcined at 1275 K for 8 h to decompose the carbonate. Then, the product was reground and pressed into pellets, sintered in air for two periods of 48 h at 1653 K with intermediate grinding and pelletizing. $Ca_{2-x}Mn_xMnTaO_6$ samples with x = 0.2, 0.4, 0.6, 0.8, 1.0, 1.5, 1.6 and 2.0 were synthesized from the stoichiometric mixtures of the as-prepared CMTO, MnO (Alfa Aesar, 99.99%), Mn_2O_3, and Ta_2O_5. Samples with x = 0.2 were heated at 1625 K for 24 h under ambient pressure (AP), whereas x = 0.4 - 2.0 were prepared in a Walker-type multi-anvil apparatus at 1523-1625 K under 5-8 GPa for 30 min in Pt capsules and then quenched to room temperature, followed by a gradual release of the pressure. Around 0.5 g and 80 mg sample can be prepared for each run below and above 5 GPa, respectively, in our syntheses.

X-ray Powder Diffraction and Energy Dispersive X-ray Spectroscopy

X-ray powder diffraction (XRD) data were collected at room temperature on a RIGAKU RINT-2000 diffractometer using Cu-Kα radiation (λ = 1.5418 Å). Here the 2θ range between 10° and 120° with a step size of 0.02° was measured, using a counting time of 3.93 s per step at 40 kV and 26 mA. The TOPAS 4.2 software package[62] was applied to perform diffraction data analysis and Rietveld refinement. Cross sectional scanning electron microscopy (SEM) with energy-dispersive X-ray spectroscopy (EDS) images were recorded using a FEI Quanta 400F with an Oxford-instruments INCA 400 EDS detector operating at an accelerating voltage of 20 kV. EDS elemental composition could be expressed quantitatively as weight percentage or atomic percentage.

X-ray Absorption Near Edge and Photoelectron Spectroscopy

Mn-K and Ta-$L_{2,3}$ X-ray absorption near edge spectroscopy (XANES) data were collected in both the fluorescence and the transmission modes with simultaneous standards. All of the spectra were fit to linear pre- and post-edge backgrounds and normalized to the unity absorption step across the edge.[13, 63, 64] The $Ca_{1.8}Mn_{0.2}MnTaO_6$ XANES measurements was performed on at the Brookhaven NSLS-II on the QAS 7-BM beamline using a Si-111 channel cut monochromator. Most of the standard spectra were performed at X-19A at NSLS-I with a Si-111 double crystal monochromator. X-ray photoelectron spectroscopy (XPS) was performed on a Nexsa XPS system equipped with a monochromatic Al *Kα* X-ray source ($h\nu$ = 1486.6 eV) operated at 720 W, and background pressure was kept about 2×10^{-9} mbar. All binding energies were calibrated using surface contaminant carbon (C 1*s* = 284.8 eV) as a standard to scale.

Magnetic Measurements

Magnetic measurements were implemented with a Physical Properties Measurement System (PPMS, Quantum Design). The temperature-dependent magnetization was measured in zero field cooled (ZFC) and field cooled (FC) modes in a temperature scope of 5-400 K under 0.1 T magnetic field (H). Field dependence of isothermal magnetization was measured under an applied magnetic field varying from -5 to 5 T between 5 and 300 K.

Results and discussion

Synthesis and Structural Characterization

The degree of cationic ordering and octahedral tilting in double perovskite oxides kinetically depends on synthetic conditions as in Ca_2MnTaO_6, which was reported to be monoclinic $P2_1/m$ (No. 11, ordered Mn and Ta at the *B*-sites)[65] or the competitive orthorhombic *Pbnm* (disordering arrangement of Mn and Ta)[66] by different researchers. In our cases, all the $Ca_{2-x}Mn_xMnTaO_6$ ($0 \leq x \leq 2.0$) samples synthesized under AP and HP display black colour. Both the x = 0 and 0.2 phases can be stabilized by chemical pressure only and synthesized under AP with a better

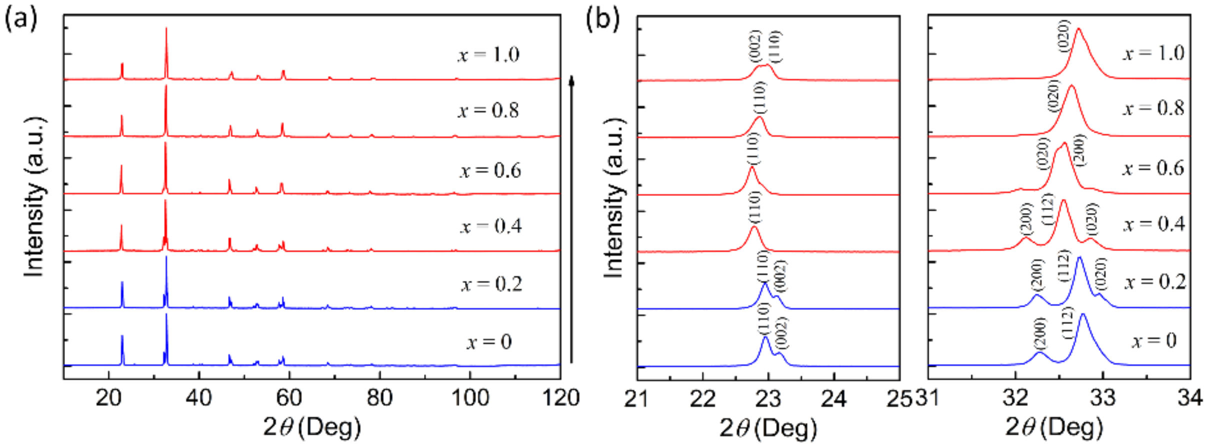

Fig. 2 (a) XRD patterns of $Ca_{2-x}Mn_xMnTaO_6$ with x = 0, 0.2, 0.4, 0.6, 0.8 and 1.0, where blue and red lines denote the phase prepared at AP and HP, respectively. (b) The enlarged XRD patterns between 21°-25° (left) and 31°-34° (right) ranges.

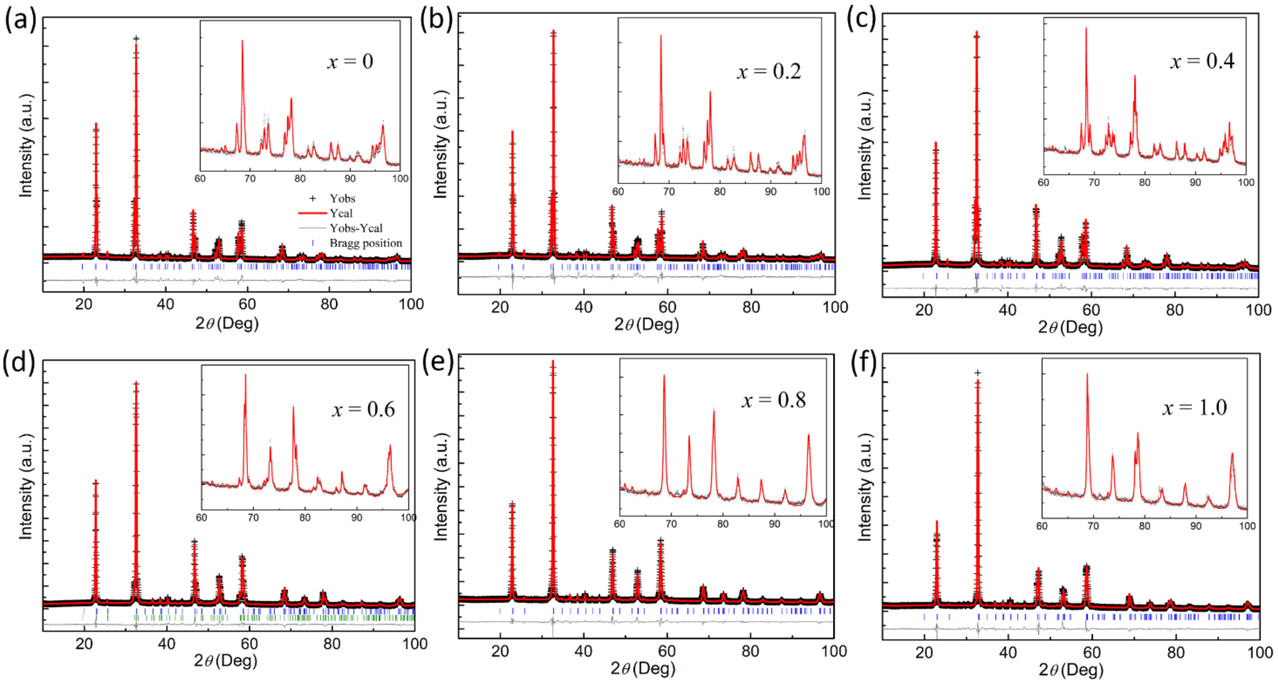

Fig. 3 Rietveld refinement of XRD patterns of $Ca_{2-x}Mn_xMnTaO_6$: (a) x = 0; (b) x = 0.2; (c) x = 0.4; (d) x = 0.6; (e) x = 0.8; (f) x = 1.0. The insets (60-100°) show enlarged views.

explanation in orthorhombic *Pbnm* from the XRD patterns (**Fig. 2a**). The chemical pressure alone is not enough to stabilize the x = 0.4 and 0.6 samples, since impurity peaks are observed beside the target phase as shown in **Fig. S1a** and **c**. Attempts to purify x = 0.4 and 0.6 series with additional physical pressures between 2 and 5 GPa were unsuccessful, since the impurity phases can be suppressed at higher pressure but are still distinct in XRD patterns of the 5 GPa products (**Fig. S1b** and **d**). Therefore, higher physical pressure is required to stabilize and drive pure phase with x above 0.4. **Fig. 2a** clearly shows that the pure orthorhombic phase can be obtained for $0.4 \le x \le 1.0$ at 7 GPa. The chemical composition of selected (x = 0.4-1.0) specimen were confirmed by EDS analyses (**Table S1**). No single phase was achieved for x above 1.5 up to 8 GPa as shown in **Fig. S1e-i**, where MnO and $Mn_3Ta_2O_8$ related phases are dominated in the x = 2.0 (Mn_2MnTaO_6) trial (**Fig. S1h** and **i**). Conclusively, chemical pressure can adequately entangle Mn^{2+} at the Ca^{2+} site in $Ca_{2-x}Mn_xMnTaO_6$ for x around 0.2, and addition physical pressure of 7 GPa can assist to pump the phase boundary (x) around 1.0 ($CaMnMnTaO_6$) but less than 1.5 ($Ca_{0.5}Mn_{1.5}MnTaO_6$). Single phase in different structure type(s) may exist at higher pressure for x > 1.0 in $Ca_{2-x}Mn_xMnTaO_6$, which is, however, not the theme of this work.

The XRD peak evolution of $Ca_{2-x}Mn_xMnTaO_6$ is highlighted in the enlarged 2θ area between 21°-25° and 31°-34° in **Fig. 2b**, respectively. The peaks continuously shift toward higher degree (right) with increasing x, suggesting successful incorporation of Mn^{2+} into the Ca^{2+} sites regarding their ionic radius difference. The main peak between 32-33° is somewhat broadened in the x = 0.6 case compared with others, suggesting symmetry degrading or the coexistence of two phases with very similar unit cell parameters. The structure refinements were

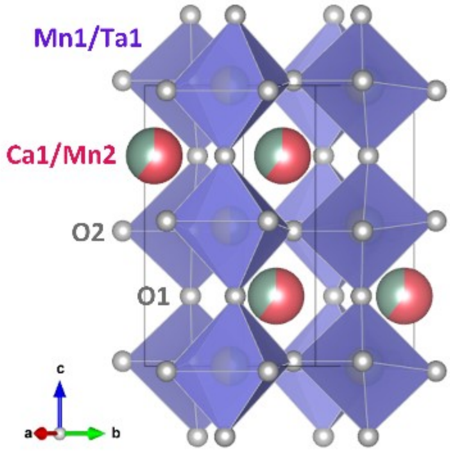

Fig. 4 Crystal structure of $Ca_{2-x}Mn_xMnTaO_6$. Ca1/Mn2 are located at the *A* site and Mn1/Ta1 are disordered over the *B* site, the violet octahedra are $(Mn1,Ta)O_6$.

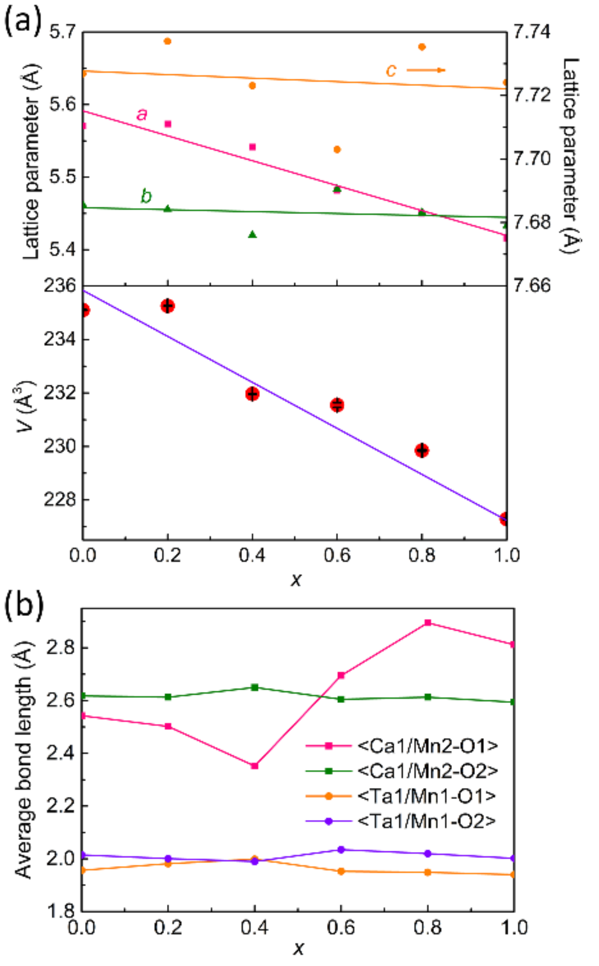

Fig. 5 Mn^{2+} ion concentration dependence of (a) the orthorhombic lattice parameter *a*(Å), *b*(Å), *c*(Å), the unit cell volume *V*(Å³), and (b) average bond lengths in $Ca_{2-x}Mn_xMnTaO_6$ refined from XRD data.

conducted for all x = 0-1.0 samples as shown in **Fig. 3**, and the corresponding crystal structures are present in **Fig. 4**. The crystal structures, besides x = 0.6, can be well refined in orthorhombic cell (*Pbnm*) starting from the model of La_2MgTiO_6.[67] The supercell of $Ca_{2-x}Mn_xMnTaO_6$ is around $\sqrt{2}a_p \times \sqrt{2}a_p \times 2a_p$, where a_p is the lattice parameter of simple cubic perovskite (~ 3.86 Å). XRD patterns of $x = 0.6$ sample can be well fitted by two *Pbnm* phases with similar cell parameters, which appeared to be x around 0.51(1) ($Ca_{1.49(1)}Mn_{0.51(1)}MnTaO_6$, 57(5)% by weight) and 0.32(1) ($Ca_{1.68(1)}Mn_{0.32(1)}MnTaO_6$, 43(7)% by weight) phases if extrapolated from the x-dependent orthorhombic lattice parameter *a*, *b*, and *c* evolution diagram in **Fig. 5a**. In the initial structural model, sites of La and Mg/Ti ions in La_2MgTiO_6 were replaced by Ca/Mn and Mn/Ta ions, respectively, with fixed occupancies according to the suggested chemical formula. The refined structural parameters and the coordinates of atoms are shown in **Table S2**, and selected bond lengths and $(Mn1/Ta1)O_6$ octahedral distortion parameters are listed in **Table S3**. Although XRD data analyses show cationic disordering at both the *A*- and *B*-sites, there must be short-range local ordering driven by the atomic potential fields, giving the size and/or charge difference between Ca/Mn and Mn/Ta. This very locally short-range ordering is highly disordered and distributed in random, and is not enough to break the overall *Pbnm* symmetry but renders relatively high atomic displacement parameters of cations (**Table S2**). Otherwise, superstructure peaks of the monoclinic structure would appear. Cationic ordering may arise in the high-pressure made $Ca_{2-x}Mn_xMnTaO_6$ if it is cooled down slowly in the synthesis procedure as reported in $CaCu_3Fe_2Nb_2O_{12}$.[37] The unit-cell dimension evolution loosely follows Vegard's law (**Fig. 5a**),[68] and the deviation may be attributed to the effect of physical pressure. The average bond lengths of (Ca1/Mn2)-O1, (Ca1/Mn2)-O2, (Ta1/Mn1)-O1, and (Ta1/Mn1)-O2 show small fluctuations (**Fig. 5b**), which is unobvious to state shortened ionic bond length under chemical pressure. The bond valence sums (BVS) calculations suggest that, the *A*-site (Ca1/Mn2) is under bonded with increasing x, while the *B*-site (Mn1/Ta1) is over bonded. To further confirm the formal oxidation state of cations in $Ca_{2-x}Mn_xMnTaO_6$, XANES and XPS measurements were conducted for selected samples.

XANES and XPS Analyses

The Mn-K main edge of $Ca_{1.8}Mn_{0.2}MnTaO_6$ is shown in **Fig. 6a** along with a series of standard spectra for comparison[69-71]. The $Sr_2Mn^{2+}ReO_6$, and $Ca_2Mn^{3+}TaO_6$ and $CaMn^{4+}O_3$ spectra illustrate the systematic "chemical shift" of the Mn-K edge, for Mn on the perovskite *B*-site, to higher energy with increasing formal Mn-valence.[69-71] The $Mn^{2+}{}_2FeReO_6$ spectrum, on the other hand, illustrates the much lower energy onset and peak typical for Mn^{2+} on the perovskite *A*-site.[63, 72] Close inspection of the $Ca_{1.8}Mn_{0.2}MnTaO_6$ spectrum indicates: a dominant perovskite-*B*-Mn^{3+} component based on the proximity of the main peak to that of $Ca_2Mn^{3+}TaO_6$; and a much smaller perovskite-*A*-Mn^{2+} component based on the excess spectral weight below the peak in the energy range where the $Mn^{2+}{}_2FeReO_6$ spectrum peaks lie. To emphasize this difference, spectrum (Diff. Spect. in the **Fig. 6a**-top) was calculated by first subtracting the appropriately weighted $Ca_2Mn^{3+}TaO_6$ spectrum from the $Ca_{1.8}Mn_{0.2}MnTaO_6$ spectrum and the results were normalized to the standard unity absorption across the edge. Despite the crudeness of this

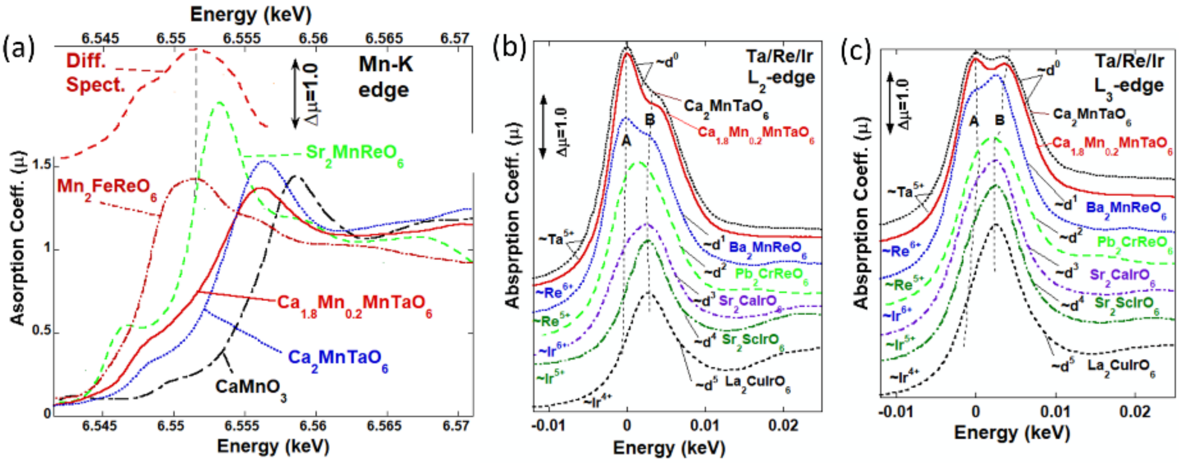

Fig. 6 (a) The Mn−K edge spectra for $Ca_{1.8}Mn_{0.2}MnTaO_6$, compared with those of a series of standard compound spectra: the *A*-site perovskite based $Mn^{2+}{}_2FeReO_6$; the *B*-site perovskite based $Sr_2Mn^{2+}ReO_6$, $Ca_2Mn^{3+}TaO_6$ and $CaMn^{4+}O_3$. The spectrum labeled as "Diff. Spect." is a weighted difference spectrum (with normalization) to estimate the *A* site Mn spectrum in $Ca_{1.8}Mn_{0.2}MnTaO_6$. (b) A superimposed comparison of the Ta-L_2 and L_3 edge of $Ca_{1.8}Mn_{0.2}MnTaO_6$ to those of the d^0/Ta^{5+}-Ca_2MnTaO_6, d^1/Re^{6+}-Ba_2MnReO_6, d^2/Re^{5+}-Pb_2CrReO_6, d^3/Ir^{6+}-Sr_2CaIrO_6, d^4/Ir^{5+}-Sr_2ScIrO_6 and d^5/Ir^{4+}-La_2CuIrO_6 standards, indicating Ta^{5+} in $Ca_{1.8}Mn_{0.2}MnTaO_6$.

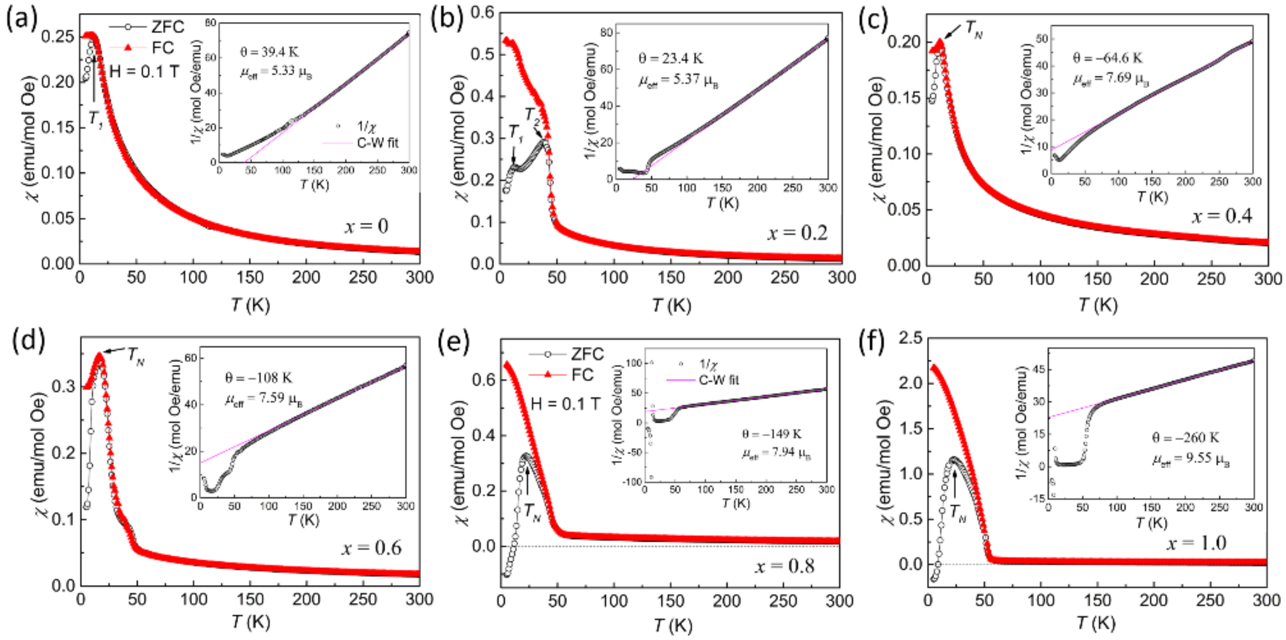

Fig. 7 Magnetic properties of $Ca_{2-x}Mn_xMnTaO_6$. Temperature dependence of the magnetic susceptibilities measured at 0.1 T under zero-field-cooled (ZFC, empty circles) and field-cooled (FC, filled triangles) conditions between 5 and 300 K. (a) $x = 0$; (b) $x = 0.2$; (c) $x = 0.4$; (d) $x = 0.6$; (e) $x = 0.8$; (f) $x = 1$. The insets show the ZFC χ^{-1} *vs* *T* curves at 0.1 T with the Curie−Weiss fits.

approximation the difference spectrum manifests a very clear spectral peak at precisely the peak energy of the perovskite-*A*-site standard $Mn^{2+}{}_2FeReO_6$. Thus, there is a strong conclusion that the Mn-K edge results support the ~Mn^{3+} (perovskite-*B*-site) and ~Mn^{2+} (perovskite-*A*-site) assignments respectively for the Mn and $Mn_{0.2}$ components in the $Ca_{1.8}Mn_{0.2}MnTaO_6$ compound formula.

The prominent bimodal A/B peak features in 5*d*-row $L_{2,3}$ edge features, in octahedrally coordinated oxides, have been useful probes of *d*-configuration/valence by virtue of the systematic decrease in the A (t_{2g}-hole related) feature intensity, relative to that of the B (e_g-hole related) feature. The systematic A-feature spectral weight decrease with increasing *d*-count (decreasing t_{2g}-hole count) is clearly illustrated in **Fig. 6b-c** for standard 5*d*-row compounds between d^0 and d^5.[69, 70, 73, 74] The Ta-$L_{2,3}$ edge spectra of $Ca_{1.8}Mn_{0.2}MnTaO_6$ is plotted as a solid red line in **Fig. 6b-c** and its large A-feature intensity very clearly supports the d^0/Ta^{5+} configuration/valence assignment for this compound. In summary the XANES results for $Ca_{1.8}Mn_{0.2}MnTaO_6$, manifest an *A*-site ~Mn^{2+} state, a *B*-site ~Mn^{3+} state, and a *B′*-site d^0/Ta^{5+} state.

As shown in **Fig. S2**, the XPS spectrum for Mn $2p_{3/2}$ region of $CaMnMnTaO_6$ (x = 1.0) was recorded and fitted by using XPS standard software. The spectrum exhibits three main peaks at about 640.6, 641.8, and 644.0 eV, respectively. The binding energy values are in good agreement with Mn^{2+}, Mn^{3+}, and Mn^{4+} oxidation states as reported in the literature.[75, 76] It should be pointed out that Mn^{2+} is attributed to *A*-site Mn ions and Mn^{3+}

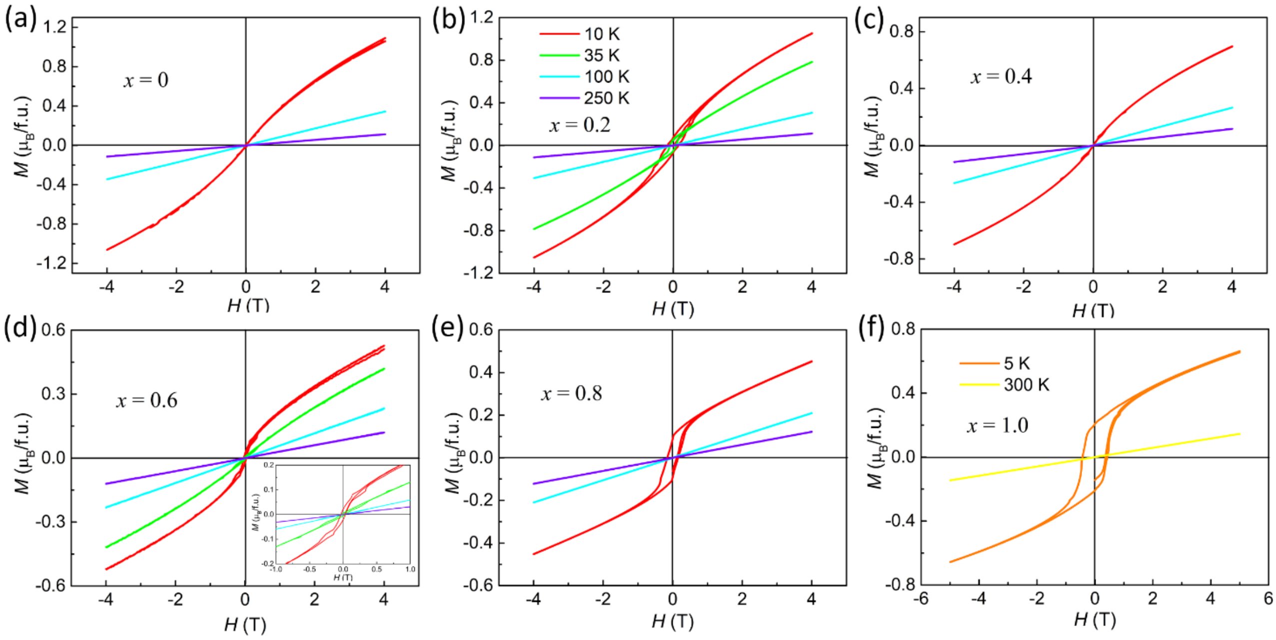

Fig. 8 Isothermal magnetization curves of $Ca_{2-x}Mn_xMnTaO_6$ at 10, 35, 100, and 250 K between -4 and 4 T. (a) $x = 0$; (b) $x = 0.2$; (c) $x = 0.4$; (d) $x = 0.6$; (e) $x = 0.8$; (f) $x = 1$. The inset in (d) shows the expanded region between -1.0 and 1.0 T, showing clear hysteresis loops at different temperatures.

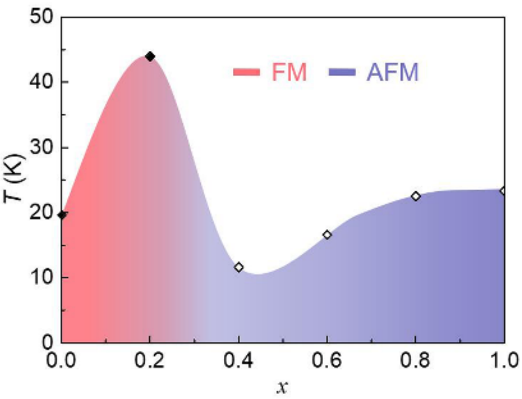

Fig. 9 Schematic magnetic phase diagram of $Ca_{2-x}Mn_xMnTaO_6$. The symbols are transition temperatures of $Ca_{2-x}Mn_xMnTaO_6$ (filled diamonds for T_C $0 \le x \le 0.2$, open diamonds for T_N of $0.4 \le x \le 1.0$). Pink area is for ferromagnetic (FM) phase, blue area for antiferromagnetic (AFM) phase.

corresponds to *B*-site Mn ions. The appearance of Mn^{4+} could derive from charge disproportionation of Mn^{3+} into Mn^{2+} and Mn^{4+} at *B*-sites.[77, 78] Based on the calculated percentage XPS peak areas, the amount of Mn^{2+}, Mn^{3+} and Mn^{4+} has been summarized in **Table S4**, which suggests that the appearance of 10% of Mn^{4+} and Mn^{2+}, respectively, from the divergence of 20% of Mn^{3+}.

Magnetic Characterization

Fig. 7 shows the temperature-dependent ZFC and FC magnetic susceptibilities (χ) for x = 0-1.0 samples measured at 0.1 T. The paramagnetic susceptibility data were fitted to the Curie-Weiss (CW) law $\chi = C/(T - \theta)$ at temperature above 150 K, where $C = \mu_{eff}^2/8$ is Curie constant, θ is Weiss temperature, and μ_{eff} is effective magnetic moment. In **Fig. 7a**, the resulting θ = 39.4 K for $x = 0$ indicates that the predominant magnetic interactions are ferromagnetic (FM) transition. The divergence between FC and ZFC data in the magnetic susceptibility at T_1 = 19.6 K suggests FM transition temperature. It also implies that magnetic transition is due to spin-only Mn^{3+} (S = 2) and Mn^{3+}-O^{2-}-Mn^{3+} super-exchange interactions corresponding to μ_{eff} = 5.33 μ_B/f.u.. It needs to be mentioned that an anomaly transition appearing around 114 K is due to measuring instrument problem. As shown in **Fig. 7b**, it clearly exhibits two magnetic transitions with $x = 0.2$: the temperature at T_1 = 19.6 K is nearly identical to x = 0, and it is the result of the spin magnetization of Mn^{3+} at *B* site; on account of the doping of Mn^{2+} at *A* site, FM transition appeared at T_2 = 44 K. The effective magnetic moment (μ_{eff} = 5.37 μ_B) could be obtained by CW law fitting, which is close to the theoretical value (5.57 μ_B) corresponding to spin-only *A* site Mn^{2+} (high spin d^5) and *B* site Mn^{3+} (high spin d^4) moments as evidenced by the crystal structure and XANES results. With the increasing of dopant, the samples of x = 0.4, 0.6, 0.8 and 1.0 phases display an antiferromagnetic (AFM) state as shown in **Fig. 7c-f**. A significant peak in the ZFC curve suggests the onset of an antiferromagnetic transition at T_N. It is noteworthy that the magnitudes of their negative Weiss temperatures are much higher than T_N, suggesting significant magnetic frustration/interaction. The substitution of Ca^{2+} ions by Mn^{2+} can be defined as the “chemical pressure”, which can be attributed to the decrease of magnetic transition temperature.[79, 80] Their effective magnetic moments are greater than the calculated values due to magnetic interactions between Mn^{2+} and Mn^{3+}. As exhibited in **Fig. 7e-f**, another interesting finding is that a negative ZFC $\chi(T)$ is observed in the x = 0.8 and 1.0 samples. This has been proposed in the literature that misplaced *B*-site cations can result in the antiphase boundary coming into being, which is accompanied by a short-ranged FM coupling between Mn^{2+} and Mn^{4+} ions at *B* sites as evidenced by XPS results, and an AFM coupling occurs in the antiphase boundary. In the ZFC mode, the magnetic field of 0.1 T is insufficient to align all frozen clusters and domain spins in the direction of field. By this sense, as the temperature decreases, the spin anti-parallel or tilt state is stabilized, resulting in the residual magnetization tends to be negative. A similar phenomenon occurred in R_2NiMnO_6 (R = Pr, Nd, Y, and Ho) and $La_{2-x}Bi_xCoMnO_6$ (x = 0 and 0.1).[81, 82]

The isothermal magnetization $M(H)$ was measured at different temperatures from 5 to 300 K under magnetic field between -5 and 5 T. The $M(H)$ results presented in **Fig. 8** support this conclusion with the magnetic hysteresis loop below T = 10 K, most dramatically evidencing a first-order increasing-field-induced transition out of the AFM state. Samples of x = 0 and 0.4 show *S*-type shape curves in 10 K, which reflected typical weak canted ferromagnetism, displayed in **Fig. 8a** and **c**, respectively. As shown in Fig. 8b, a hysteresis loop is present in x = 0.2 down to the temperature measured (T = 35 K), which confirms the presence of FM ordering below the FM transition at T_C = 44 K, and present even at low temperatures. The other AFM samples also showed a clear hysteresis loop at 10 K given in **Fig. 8d-f**. Their FM properties appeared owing to the concentration of induced magnetic moments on Mn at the *A* site increasing. The magnetic parameters of the CW law fitting of $Ca_{2-x}Mn_xMnTaO_6$ system with $0 \le x \le 1.0$ were summarized in **Table S5**, and have been used to map the magnetic phase diagram as shown in **Fig. 9**. Samples of x = 0 and 0.2 were FM dominated phases with T_C = 19.6 and 44 K, respectively. It can be found in $Ca_{2-x}Mn_xMnTaO_6$ for $0.4 \le x \le 1.0$ that Mn^{2+} at the *A* site involved in the long-range magnetic order and enhances the AFM order Mn-O-Mn super-exchange with increment of x, and T_N gradually becomes larger and tends to be constant.

Unlike the other exotic perovskite with 50% of the *A*-site occupied by transition metal cations, such as the *A*-site columnar-ordered $P4_2/n$-type quadruple perovskites $CaMnBReO_6$ (B = Mn,[20] Fe,[20] Co,[21] Ni[21]), $CaMn_{0.5}Cu_{0.5}FeReO_6$,[20] and $RMnMnSbO_6$ (R = La, Pr, Nd, Sm),[22] and $P4_2mc$ structural $Ca_{1.4}Mn_{0.6}Ti_2O_6$ in $Ca_{2-x}Mn_xTi_2O_6$ ($x \le 0.6$),[19] either *A*- or *B*-site cationic ordering is absent in $Ca_{2-x}Mn_xMnTaO_6$, and the structural formula can be written as $(Ca_{1-x/2}Mn_{x/2})(Mn_{0.5}Ta_{0.5})O_3$, namely $(Ca^{2+}_{0.5}Mn^{2+}_{0.5})(Mn^{3+}_{0.5}Ta^{5+}_{0.5})O_3$ other than $CaMnMnTaO_6$ for x = 1.0, which is, to the best of our knowledge, for the first time observed in exotic perovskite with half of the *A*-site occupied by small transition metal ions. In $Ca_{2-x}Mn_xTi_2O_6$ prepared under chemical and soft physical pressure, similar *A*-site Ca/Mn disordering was observed for x below 0.4. However, *A*-site columnar-ordered quadruple perovskite $A_2A'A''B_4O_{12}$ is obtained for $Ca_{2-x}Mn_xTi_2O_6$ with $0.4 \le x \le 0.6$.[19] When Ti^{4+} was replaced by Mn/Ta in $Ca_{2-x}Mn_xTi_2O_6$, the *A*-site columnar-ordered vanished in this work. Probably, the coexistence of *B*-site Mn^{3+} (Jahn-Teller distortion ion) and *B*'-site Ta^{5+} (second-order Jahn-Teller distortion ion) does not favour the formation of *A*-site columnar ordered perovskite structure $(Ca)^{A}{}_2(Mn)^{A'}(Mn)^{A''}(Mn)^{B}{}_2\ (Ta)^{B'}{}_2O_{12}$ (x = 1.0 case), and the cationic disordering at both the *A*- and *B*-sites, together with charge disproportionation of Mn^{3+} into Mn^{2+} and Mn^{4+} at the *B*-sites, synergically renders a lower energy ground state in *Pbnm* structure in $Ca_{2-x}Mn_xMnTaO_6$.

Conclusions

In conclusion, we have prepared new exotic perovskite oxides $Ca_{2-x}Mn_xMnTaO_6$ ($0 \le x \le 1.0$) by means of combining chemical and physical pressure technique. The lower-Mn compounds ($x \le 0.2$) can be solely stabilized by chemical pressure, while the target phase dominated samples can be achieved at intermediate physical pressure of 7 GPa for $0.4 \le x \le 1.0$. The crystal structure remains *Pbnm* as in Ca_2MnTaO_6, and can be structurally written as $(Ca_{1-x/2}Mn_{x/2})(Mn_{1/2}Ta_{1/2})O_3$ without expected *A*-site columnar-ordering. Both the X-ray absorption near edge and photoelectric spectroscopy data suggested $Ca_{2-x}Mn^{2+}{}_xMn^{3+}Ta^{5+}O_6$ ($0 \le x \le 0.6$) and $Ca_{2-x}Mn^{2+}{}_x(Mn^{3+,2+/4+})Ta^{5+}O_6$ ($0.8 \le x \le 1.0$). The spin-only *A* site Mn^{2+} (high spin d^5) and *B* site Mn^{3+} (high spin d^4) moments enhance a ferromagnetic ($x \le 0.2$) to antiferromagnetic ($0.4 \le x \le 1.0$) transition around the boundary of x = 0.2. The partial charge disproportionation of the *B*-site Mn^{3+} into Mn^{2+} and Mn^{4+} x = 0.8 and 1.0 introduces negative ZFC magnetization stemming from the formation of spin antiparallel or ferromagnetic clusters and domains separating by the antiphase boundaries. This charge disproportionation over the *B*-sites could have synergic contribution to stabilize the highly disordered *Pbnm* structure in $Ca_{2-x}Mn_xMnTaO_6$.The present findings updated the fundamental understanding of fixing of high-pressure phase within an ambient-pressure phase matrix, and implied that the coexistence of Jahn-Teller distorted ions at the *B*- and *B*'-sites should be avoided in $A_2A'A''B_2B'_2O_{12}$ to ensure cationic ordering and strong magnetic interactions.

Conflicts of interest

There are no conflicts to declare.

Acknowledgements

This work was financially supported by the National Science Foundation of China (NSFC-21801253, 11804404, and 21875287) and the National Science Foundation (NSF) Grant No. DMR-1809931. Structural analysis of exotic materials in this study was partly supported by the Research Grant No. 075-15-2019-1886 from the Government of the Russian Federation. The XANES work at the Brookhaven National Laboratory, NSLS-II was supported by the DOEBES (DE-SC0012704). The NSLS-II work was performed on beamline 7-BM and the authors gratefully acknowledge the invaluable help of the beamline scientists Steven Ehrlich and Syed Khalid.

Notes and references

1. M. A. Peña and J. L. G. Fierro, *Chem. Rev.*, 2001, **101**, 1981-2018.
2. B. Raveau, Prog. *Solid State Chem.*, 2007, **35**, 171-173.

3. S. Vasala and M. Karppinen, *Prog. Solid State Chem.*, 2015, **43**, 1-36.
4. D. Serrate, J. M. D. Teresa and M. R. Ibarra, *J. Phys.: Condens. Matter*, 2007, **19**, 023201.
5. V. M. Goldschmidt, *Die Naturwissenschaften*, 1926, **14**, 477–485.
6. W. Li, E. Ionescu, R. Riedel and A. Gurlo, *J. Mater. Chem. A*, 2013, **1**, 12239-12245.
7. D. Beqiri, V. Cascos, J. Roberts-Watts, E. R. Clark, E. Bousquet, N. C. Bristowe and E. E. McCabe, *Chem. Commun.*, 2019, **55**, 2609-2612.
8. C. J. Bartel, C. Sutton, B. R. Goldsmith, R. Ouyang, C. B. Musgrave, L. M. Ghiringhelli and M. Scheffler, *Sci. Adv.*, 2019, **5**, eaav0693.
9. M. R. Filip and F. Giustino, *Proc. Natl. Acad. Sci.*, 2018, **115**, 5397.
10. H. Zhang, N. Li, K. Li and D. Xue, *Acta Crystallogr. Sec. B*, 2007, **63**, 812-818.
11. P. W. Barnes, M. W. Lufaso and P. M. Woodward, *Acta Crystallogr. B*, 2006, **62**, 384-396.
12. M. W. Lufaso and P. M. Woodward, *Acta Crystallogr. B*, 2004, **60**, 10-20.
13. M.-R. Li, P. W. Stephens, M. Croft, Z. Deng, W. Li, C. Jin, M. Retuerto, J. P. Hodges, C. E. Frank, M. Wu, D. Walker and M. Greenblatt, *Chem. Mater.*, 2018, **30**, 4508-4514.
14. M.-R. Li, J. P. Hodges, M. Retuerto, Z. Deng, P. W. Stephens, M. C. Croft, X. Deng, G. Kotliar, J. Sánchez-Benítez, D. Walker and M. Greenblatt, *Chem. Mater.*, 2016, **28**, 3148-3158.
15. M.-R. Li, M. Retuerto, Z. Deng, P. W. Stephens, M. Croft, Q. Huang, H. Wu, X. Deng, G. Kotliar, J. Sánchez-Benítez, J. Hadermann, D. Walker and M. Greenblatt, *Angew. Chem. Int. Ed.*, 2015, **54**, 12069-12073.
16. A. Hossain, P. Bandyopadhyay and S. Roy, *J. Alloys Compd.*, 2018, **740**, 414-427.
17. K. Leinenweber and J. Parise, *J. Solid State Chem.*, 1995, **114**, 277-281.
18. A. Aimi, D. Mori, K.-i. Hiraki, T. Takahashi, Y. J. Shan, Y. Shirako, J. Zhou and Y. Inaguma, *Chem. Mater.*, 2014, **26**, 2601-2608.
19. Z. Li, Y. Cho, X. Li, X. Li, A. Aimi, Y. Inaguma, J. A. Alonso, M. T. Fernandez-Diaz, J. Yan, M. C. Downer, G. Henkelman, J. B. Goodenough and J. Zhou, *J. Am. Chem. Soc.*, 2018, **140**, 2214-2220.
20. G. M. McNally, Á. M. Arévalo-López, P. Kearins, F. Orlandi, P. Manuel and J. P. Attfield, *Chem. Mater.*, 2017, **29**, 8870-8874.
21. E. Solana-Madruga, Y. Sun, Á. M. Arévalo-López and J. P. Attfield, *Chem. Commun.*, 2019, **55**, 2605-2608.
22. E. Solana-Madruga, Á. M. Arévalo-López, A. J. Dos Santos-García, E. Urones-Garrote, D. Ávila-Brande, R. Sáez-Puche and J. P. Attfield, *Angew. Chem. Int. Ed.*, 2016, **55**, 9340-9344.
23. A. A. Belik, *Dalton Trans.*, 2018, **47**, 3209-3217.
24. A. A. Belik, L. Zhang, Y. Matsushita, Y. Katsuya, M. Tanaka and K. Yamaura, *J. Solid State Chem.*, 2019, **275**, 43-48.
25. A. A. Belik, D. D. Khalyavin, L. Zhang, Y. Matsushita, Y. Katsuya, M. Tanaka, R. D. Johnson and K. Yamaura, *ChemPhysChem*, 2018, **19**, 2449-2452.
26. L. Zhang, Y. Matsushita, K. Yamaura and A. A. Belik, *Inorg. Chem.*, 2017, **56**, 5210-5218.
27. S. Zhang, T. Saito, M. Mizumaki, W.-t. Chen, T. Tohyama and Y. Shimakawa, *J. Am. Chem. Soc.*, 2012, **135**, 6056-6060.
28. Y. W. Long, N. Hayashi, T. Saito, M. Azuma, S. Muranaka and Y. Shimakawa, *Nature*, 2009, **458**, 60-63.
29. S. V. Ovsyannikov, E. Bykova, A. Pakhomova, D. P. Kozlenko, M. Bykov, S. E. Kichanov, N. V. Morozova, I. V. Korobeinikov, F. Wilhelm, A. Rogalev, A. A. Tsirlin, A. V. Kurnosov, Y. G. Zainulin, N. I. Kadyrova, A. P. Tyutyunnik and L. Dubrovinsky, *Inorg. Chem.*, 2017, **56**, 6251-6263.
30. S. V. Ovsyannikov, Y. G. Zainulin, N. I. Kadyrova, A. P. Tyutyunnik, A. S. Semenova, D. Kasinathan, A. A. Tsirlin, N. Miyajima and A. E. Karkin, *Inorg. Chem.*, 2013, **52**, 11703-11710.
31. K. Shiro, I. Yamada, N. Ikeda, K. Ohgushi, M. Mizumaki, R. Takahashi, N. Nishiyama, T. Inoue and T. Irifune, *Inorg. Chem.*, 2013, **52**, 1604-1609.
32. S. Mehmood, Z. Ali, Z. Hashmi and S. Khan, Int. *J. Mod Phys B*, 2019, **33**. 1950212.
33. T. Locherer, R. Dinnebier, R. K. Kremer, M. Greenblatt and M. Jansen, *J. Solid State Chem.*, 2012, **190**, 277-284.
34. F. Mezzadri, M. Calicchio, E. Gilioli, R. Cabassi, F. Bolzoni, G. Calestani and F. Bissoli, *Phys. Rev. B*, 2009, **79**, 014420.
35. R. Przeniosło, I. Sosnowska, E. Suard, A. Hewat and A. N. Fitch, *Physica B: Condens. Matter*, 2004, **344**, 358-367.
36. W.-t. Chen, M. Mizumaki, H. Seki, M. S. Senn, T. Saito, D. Kan, J. P. Attfield and Y. Shimakawa, *Nat. Commun.*, 2014, **5**.
37. M. S. Senn, W.-t. Chen, T. Saito, S. García-Martín, J. P. Attfield and Y. Shimakawa, *Chem. Mater.*, 2014, **26**, 4832-4837.
38. X. Wang, M. Liu, X. Shen, Z. Liu, Z. Hu, K. Chen, P. Ohresser, L. Nataf, F. Baudelet, H.-J. Lin, C.-T. Chen, Y.-L. Soo, Y.-f. Yang, C. Jin and Y. Long, *Inorg. Chem.*, 2019, **58**, 320-326.
39. A. Prodi, E. Gilioli, R. Cabassi, F. Bolzoni, F. Licci, Q. Huang, J. W. Lynn, M. Affronte, A. Gauzzi and M. Marezio, *Phys. Rev. B*, 2009, **79**, 085105.
40. F. Mezzadri, G. Calestani, M. Calicchio, E. Gilioli, F. Bolzoni, R. Cabassi, M. Marezio and A. Migliori, *Phys. Rev. B*, 2009, **79**, 100106.
41. A. A. Belik, Y. Matsushita, Y. Kumagai, Y. Katsuya, M. Tanaka, S. Y. Stefanovich, B. I. Lazoryak, F. Oba and K. Yamaura, *Inorg. Chem.*, 2017, **56**, 12272-12281.
42. T. Kawamoto, K. Fujita, I. Yamada, T. Matoba, S. J. Kim, P. Gao, X. Pan, S. D. Findlay, C. Tassel, H. Kageyama, A. J. Studer, J. Hester, T. Irifune, H. Akamatsu and K. Tanaka, *J. Am. Chem. Soc.*, 2014, **136**, 15291-15299.
43. L. Liu, H. X. Song, X. Li, D. Zhang, R. Mathieu, S. Ivanov, H. Skogby and P. Lazor, *Appl. Phys. Lett.*, 2019, **114**, 162903.
44. H.-P. Su, S.-F. Li, Y. Han, M.-X. Wu, C. Gui, Y. Chang, M. Croft, S. Ehrlich, S. Khalid, U. Adem, S. Dong, Y. Sun, F. Huang and M.-R. Li, *J. Mater. Chem. C*, 2019, **7**, 12306-12311.
45. M. Markkula, A. M. Arevalo-Lopez, A. Kusmartseva, J. A. Rodgers, C. Ritter, H. Wu and J. P. Attfield, *Phys. Rev. B*, 2011, **84**, 094450.
46. A. A. Belik, Y. Matsushita, M. Tanaka and E. Takayama-Muromachi, *Chem. Mater.*, 2012, **24**, 2197-2203.
47. A. B. Alexei and Y. Wei, *J. Phys.: Condens. Matter*, 2014, **26**, 163201.
48. E. Solana-Madruga, A. J. Dos santos-Garcia, A. M. Arevalo-Lopez, D. Avila-Brande, C. Ritter, J. P. Attfield and R. Saez-Puche, *Dalton Trans.*, 2015, **44**, 20441-20448.
49. G. V. Bazuev, A. P. Tyutyunnik, M. V. Kuznetsov and Y. G. Zainulin, *J. Supercond. Nov. Magn.*, 2018, **31**, 2907-2914.
50. A. M. Arevalo-Lopez, F. Stegemann and J. P. Attfield, *Chem. Commun.*, 2016, **52**, 5558-5560.
51. A. M. Arévalo-López, G. M. McNally and J. P. Attfield, *Angew. Chem. Int. Ed.*, 2015, **54**, 12074-12077.
52. C. E. Frank, E. E. McCabe, F. Orlandi, P. Manuel, X. Tan, Z. Deng, M. Croft, V. Cascos, T. Emge, H. L. Feng, S. Lapidus, C. Jin, M. Wu, M. R. Li, S. Ehrlich, S. Khalid, N. Quackenbush, S. Yu, D. Walker and M. Greenblatt, *Chem. Commun.*, 2019, **55**, 3331-3334.
53. Y. Akizuki, I. Yamada, K. Fujita, K. Taga, T. Kawakami, M. Mizumaki and K. Tanaka, *Angew. Chem. Int. Ed.*, 2015, **54**, 10870-10874.
54. Y. Akizuki, I. Yamada, K. Fujita, N. Nishiyama, T. Irifune, T. Yajima, H. Kageyama and K. Tanaka, *Inorg. Chem.*, 2013, **52**, 11538-11543.
55. S. V. Ovsyannikov, A. M. Abakumov, A. A. Tsirlin, W. Schnelle, R. Egoavil, J. Verbeeck, G. Van Tendeloo, K. V. Glazyrin, M.

Hanfland and L. Dubrovinsky, *Angew. Chem. Int. Ed.*, 2013, **52**, 1494-1498.

56. M. Murakami, K. Hirose, K. Kawamura, N. Sata and Y. Ohishi, *Science*, 2004, **304**, 855-858.
57. J. Santillán, S.-H. Shim, G. Shen and V. B. Prakapenka, *Geophys. Res. Lett.*, 2006, **33**, L15307.
58. J. Ruiz-Fuertes, T. Bernert, D. Zimmer, N. Schrodt, M. Koch-Müller, B. Winkler, L. Bayarjargal, C. Popescu, S. MacLeod and K. Glazyrin, *Phys. Rev. B*, 2017, **96**, 094101.
59. G. Gou, N. Charles, J. Shi and J. M. Rondinelli, *Inorg. Chem.*, 2017, **56**, 11854-11861.
60. J. Li, S. Lorger, J. K. Stalick, A. W. Sleight and M. A. Subramanian, *Inorg. Chem.*, 2016, **55**, 9798-9804.
61. R. Shannon, *Acta Crystallogr. Sect. A*, 1976, **32**, 751-767.
62. Bruker AXS, Karlsruhe, Germany, 2008.
63. J. Wang, B. Wylie-van Eerd, T. Sluka, C. Sandu, M. Cantoni, X.-K. Wei, A. Kvasov, L. J. McGilly, P. Gemeiner, B. Dkhil, A. Tagantsev, J. Trodahl and N. Setter, *Nat. Mater.*, 2015, **14**, 985-990.
64. S. Ali, W. Khan, G. Murtaza, M. Yaseen, S. M. Ramay and A. Mahmood, J. Magn. Magn. Mater., 2017, **441**, 113-123.
65. T. K. Mandal, V. V. Poltavets, M. Croft and M. Greenblatt, *J. Solid State Chem.*, 2008, **181**, 2325-2331.
66. P. W. Barnes, M. W. Lufaso and P. M. Woodward, *Acta Crystallogr. Sect. B*, 2006, **62**, 384-396.
67. M. P. Seabra, M. Avdeev, V. M. Ferreira, R. C. Pullar and N. M. Alford, *J. Eur. Ceram. Soc.*, 2003, **23**, 2403-2408.
68. A. R. Denton and N. W. Ashcroft, *Phys. Rev. A*, 1991, **43**, 3161-3164.
69. G. Popov, M. Greenblatt and M. Croft, *Phys. Rev. B*, 2003, **67**, 024406.
70. T. K. Mandal, V. V. Poltavets, M. Croft and M. Greenblatt, *J. Solid State Chem.*, 2008, **181**, 2325-2331.
71. F. Bridges, C. H. Booth, G. H. Kwei, J. J. Neumeier and G. A. Sawatzky, *Phys. Rev. B*, 2000, **61**, R9237.
72. K. Zhong, B. Zhang, S. Luo, W. Wen, H. Li, X. Huang and L. Chen, *J. Power Sources*, 2011, **196**, 6802-6808.
73. M. Retuerto, M.-R. Li, P. W. Stephens, J. Sánchez-Benítez, X. Deng, G. Kotliar, M. C. Croft, A. Ignatov, D. Walker and M. Greenblatt, *Chem. Mater.*, 2015, **27**, 4450-4458.
74. M. A. Laguna-Marco, P. Kayser, J. A. Alonso, M. J. Martínez-Lope, M. van Veenendaal, Y. Choi and D. Haskel, *Phys. Rev. B*, 2015, **91**, 214433.
75. Z. Huang, W. Zhou, C. Ouyang, J. Wu, F. Zhang, J. Huang, Y. Gao and J. Chu, *Sci. Rep.*, 2015, **5**, 10899.
76. H. R. Barai, A. N. Banerjee and S. W. Joo, *J. Ind. Eng. Chem.*, 2017, **56**, 212-224.
77. M. Yonemura, T. Kohigashi, A. Yamada, N. Sonoyama, H. Kobayashi, T. Kamiyama and R. Kanno, *Electrochemistry*, 2003, **71**, 1160-1161.
78. E. Pollert, *Int. J. Inorg. Mater.*, 2000, **2**, 661-670.
79. A. A. Belik, Y. Matsushita, M. Tanaka and E. Takayama-Muromachi, *Angew. Chem. Int. Ed.*, 2010, **49**, 7723-7727.
80. A. Hauser, N. Amstutz, S. Delahaye, A. Sadki, S. Schenker, R. Sieber and M. Zerara, *Chimia*, 2002, **56**, 685-689.
81. M. Nasir, S. Kumar, N. Patra, D. Bhattacharya, S. N. Jha, D. R. Basaula, S. Bhatt, M. Khan, S.-W. Liu, S. Biring and S. Sen, *ACS Appl. Electron. Mater*., 2019, **1**, 141-153.
82. Y. Bai, Y. Xia, H. Li, L. Han, Z. Wang, X. Wu, S. Lv, X. Liu and J. Meng, *J. Phys. Chem. C.*, 2012, **116**, 16841-16847.

Magnetic Transition in Exotic Perovskites Stabilized by Chemical and Physical Pressure

Yalin Ma,[a] Maxim S. Molokeev,[b,c,d] Chuanhui Zhu,[a] Shuang Zhao,[a] Yifeng Han,[a] Meixia Wu,[a] Sizhan Liu,[e] Trevor A. Tyson,[e] Mark Croft[f] and Man-Rong Li*,[a]

Graphic Abstract

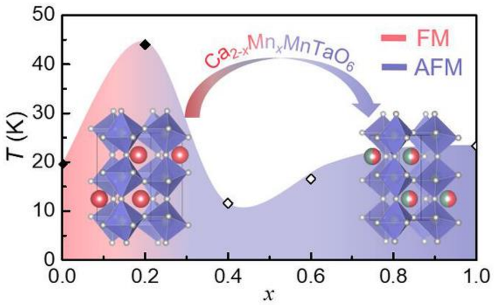

Exotic perovskite $Ca_{2-x}Mn_xMnTaO_6$ ($0 \leq x \leq 1.0$) stabilized by chemical and physical pressure adopts cationic-disordered *Pbnm* structure and exhibits a ferromagnetic to antiferromagnetic transition around $x = 0.2$.